Optically Induced Sieve Effect for Nanoparticles near a Nanofiber Taper

Mark Sadgrove,[1,*] Takaaki Yoshino,[2] Masakazu Sugawara,[2] Yasuyoshi Mitsumori,[2,3] and
Keiichi Edamatsu[2]

[1]*Department of Physics, Faculty of Science, Tokyo University of Science, 1-3 Kagurazaka, Shinjuku-ku, Tokyo
162-8601, Japan*

[2]*Research Institute of Electrical Communication, Tohoku University, Sendai 980-8577, Japan*

[3]*Department of Physics, School of Science, Kitasato University, Sagamihara 252-0373, Japan*

We demonstrate size-selective optical trapping and transport for nanoparticles near an optical nanofiber taper. Using a two-wavelength counterpropagating mode configuration, we show that 100-nm-diameter and 150-nm-diameter gold nanospheres (GNSs) are trapped by the evanescent field in the taper region at different optical powers. Conversely, when one nanoparticle species is trapped the other may be transported, leading to a sievelike effect. Our results show that sophisticated optical manipulation can be achieved in a passive configuration by taking advantage of mode behavior in nanophotonic devices.

I. INTRODUCTION

The filtering of particles by size is a requirement across a range of fields, including fabrication of artificial quantum emitters [1–4], detection and separation of biological particles [5–9], and gas separation [10]. Although mechanical techniques exist for many applications (with some remarkable recent examples [10,11]), in the nanoparticle regime, much recent effort has been focused on optical methods [12–14], due to their inherent flexibility. One aspect of optical manipulation showing promise in this area is the use of counterpropagating optical fields, which allows sophisticated particle control including optical pulling-type effects and the use of optical nonlinearity to achieve size sensitive optically induced forces [15,16].

On the other hand, a separate research avenue for the manipulation of nanosize particles of many types makes use of nanostructures including nanowaveguides [17–21] and plasmonic nanostructures [22,23]. In particular, a very recent combination of nanowaveguide techniques with the above-mentioned counterpropagating field method has led to remarkable selective control of nanodiamonds near to an optical nanofiber conditional on the number of N-*V* centers they contain [24]. This suggests that combining multiple wavelength techniques with nano-optics may prove to be fertile ground for the realization of innovative selective manipulation techniques.

Here, we make use of the mode behavior in the taper region of an optical nanofiber to achieve a dichotomous

regime where nanoparticles of one size are trapped while those of a different size are transported. This scheme constitutes a type of optical sieve but unlike a conventional sieve, either larger or smaller particles can be retained while the other species passes through. Our method is significantly different from other recent results that have demonstrated size-selective optical forces [12,14,25] in that it achieves a dichotomous transport regime with a passive configuration, by making use of the difference in variation in the radiation-pressure force as a function of wavelength for the evanescent portion of modes in the fiber taper.

II. PHYSICAL PRINCIPLES

The concept of our experiment is illustrated in Fig. 1. Colloidal gold nanospheres (GNSs) that come close to an optical-fiber taper (waist diameter 500 nm) are trapped near its surface by the gradient force F_{grad} and propelled by the absorption and scattering of photons from the evanescent portion of the fiber mode [17]. This force is F^{640} in the positive z direction due to the $+z$-propagating x-polarized 640-nm HE_{11} (fundamental) mode and F^{785} in the negative z direction due to the $-z$-propagating x-polarized 785-nm HE_{11} mode. These forces will balance at a certain power difference between the two beams, which depends on the polarizability of the particles at both wavelengths.

Inset (a) of Fig. 1 shows the forces experienced by a particle of diameter D_{GNS} on the surface of a 500-nm-diameter nanofiber for an input power of 1 mW at 640-nm wavelength (green points) and 785-nm wavelength (red
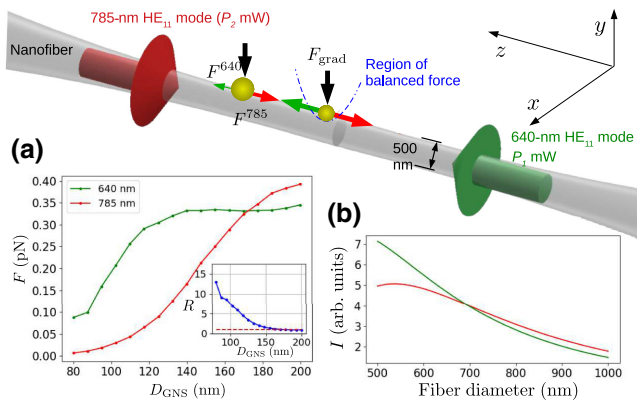
———————
*mark.sadgrove@rs.tus.ac.jp

FIG. 1. The concept and physical principles. A conceptual diagram showing the trapping and transport of 100- and 150-nm-diameter gold nanospheres along a 500-nm-diameter optical nanofiber. The green and red arrows depict the optical force due to the 640-nm HE_{11} mode and the 785-nm HE_{11} mode, respectively. Inset (a) shows FDTD-simulated force along the fiber axis for 640-nm light and 785-nm light as indicated in the legend, with the inset showing their ratio. Inset (b) shows how the light intensity at the fiber surface depends on the fiber diameter.

points). In both cases, the data points show forces evaluated using finite-difference time-domain (FDTD) simulations of the system for taper parameters matched to experimental values [see Fig. 3(a)], with lines connecting the points to guide the eye. Details of the simulations are discussed in the following section. The origin of size selectivity is apparent if we compare the ratio of forces $R = F^{640}/F^{785}$ at each wavelength as a function of the particle size, as shown in the inset. For example, comparing forces on 100- and 150-nm-diameter particles, we see that $R \approx 8.4$ and $R \approx 1.7$, respectively. This means that if we hold the power of the 785-nm mode constant, force balance will occur at a 640-nm mode power that is about $5\times$ lower for a 100-nm GNS relative to a 150-nm GNS.

Above the power for force balance, trapping occurs according to the mechanism shown in inset (b) of Fig. 1, which shows the calculated dependence of the electric field intensity at the nanofiber surface as a function of the fiber diameter for a 640-nm mode (green line) and 785-nm mode (red line). It may be seen that the two curves do not have the same gradient and cross over at a certain fiber diameter. This means that it is possible for the 640-nm mode to exert the dominant force on a particle at one fiber diameter and the 785-nm mode to exert the (oppositely directed) dominant force at a larger diameter. For tapered fibers, this behavior either leads to an unstable potential maximum or a stable (trapping) potential minimum at some point along the taper, with the trap position moving to higher diameter as the power of the 640-nm beam is increased. We will calculate the potential arising

from the light radiation-pressure force in the taper for an explicit example below.

We refer to this trap configuration as a *two-color taper trap* and note that it is distinct from two-color trapping at constant nanofiber radius, which has been extensively studied both theoretically and experimentally for atomic systems [26] and theoretically in the case of nanoparticles [19,27]. It is also distinct from methods to move nanoparticles using gradient forces due to interfering beams or modes ("conveyor-belt" methods [28–33]), because we use the balance of the light radiation pressure rather than the gradient force in the present paper.

In summary, our scheme has the following differences and advantages when compared with traditional optical-tweezer techniques. First, it uses the balance of the radiation-pressure forces of the modes rather than the gradient force used for typical trapping (here, the gradient force simply provides confinement to the fiber surface [17]). Second, by using a tapered nanowaveguide, we can take advantage of the difference in the evanescent field penetration depth for two different wavelengths to arrange a trap that occurs at a specific point on the taper where the radiation-pressure force due to the counterpropagating modes cancels. Third, because the relative mode intensity at which this cancelation occurs depends on the particle size, we can arrange that only particles of a certain size are trapped, while others are transported. Size-dependent trapping is only trivially true for conventional optical tweezers in that small particles may not be trapped due to low polarizability.

III. THEORETICAL CALCULATIONS

A. Approximate calculations in the Rayleigh regime

The particle sizes used in this experiment (diameter 100 nm and 150 nm) are too large relative to the wavelengths used (640 nm and 785 nm) for the Rayleigh approximation to hold and therefore for simple theoretical expressions for the optical forces to be calculable. For this reason, we will use the FDTD method to evaluate the optical force and optical potential experienced by the particles for the purposes of comparison with experimental results. Nonetheless, for the smaller particle size (i.e., 100-nm diameter), calculations in this approximation can act as a good order-of-magnitude check on simulations while providing physical insight. In making the Rayleigh approximation, we will assume that the field experienced by a particle is that at the surface of the fiber taper, in line with the assumption of zero particle size.

Because the use of the optical gradient and radiation-pressure forces in the evanescent field of waveguides have been known for many years [17], our calculations will focus on explaining the taper-trap effect described above. The radiation-pressure force for each wavelength is given by the sum of the absorption and scattering forces.

Following Svoboda and Block, we write [34]

$$F_{\text{scatt}} = 8\pi^3 \epsilon_m I_s \frac{|\alpha|^2}{3c\lambda^4},$$

$$F_{\text{abs}} = 2\pi \epsilon_m I_s \frac{\text{Im}(\alpha)}{\lambda c}, \qquad (1)$$

$$F = F_{\text{scatt}} + F_{\text{abs}}$$

where F_{scatt} and F_{abs} are the scattering and absorption forces, respectively, along the fiber axis, and F is the total radiation-pressure force at wavelength λ. I_s is the mode intensity at the surface of the fiber taper, α is the nanoparticle polarizability, and $\epsilon_m = \epsilon_r\epsilon_0$ is the electric permittivity of the background medium (with ϵ_0 the permittivity of free space), which is water in this case ($\epsilon_r \approx 1.33^2$). Note that the calculation of I_s can be performed using textbook expressions for the cladding portion of the fiber fundamental mode [35].

B. FDTD calculations

As mentioned above, the relatively large size of the particles used in our experiment means that, strictly speaking, the Rayleigh approximation of a point particle is invalid. Therefore, for comparison with experimental results, we perform FDTD calculations using a commercial FDTD package (Lumerical Ltd.) to determine the trapping condition for each particle. In our FDTD calculations, the force is calculated using the so-called "volumetric" method, where the Lorentz force is calculated at each point on a grid within a volume that contains the nanoparticle. More specifically, the force calculated at each point is

$$\mathbf{F}_v = \epsilon_0(\nabla \cdot \mathbf{E})\mathbf{E} - i\omega(\epsilon - \epsilon_0)\mathbf{E} \times \mathbf{B}, \qquad (2)$$

where $\mathbf{E}$ is the local electric field, $\mathbf{B}$ is the local magnetic flux density, and ϵ is the local electric permittivity. The total force on a particle within the calculation volume is the sum of forces calculated at each position. In our current study, we are interested in the z component of the force as explained above and all forces referred to below are taken to be the z component of the calculated force. Note that we use the superscripts 640 and 785 on the forces to indicate the optical forces calculated at 640 nm and 785 nm, respectively.

Figures 2(a) and 2(b) show the FDTD calculated optical force difference $\Delta F = F^{640} - F^{785}$ for the case of a 100-nm GNS (black line) and a 150-nm GNS (magenta line), with force-balance conditions for 100- and 150-nm-diameter GNSs, respectively. The nanofiber diameter is set to 500 nm. With P_2 held at 12 mW, force balance is seen to occur at 1.7 mW in the 640-nm mode for 100-nm-diameter GNSs and 8.0 mW in the 640-nm mode for 150-nm-diameter GNSs. Figure 2(c) shows the force ΔF on a 100-nm-diameter GNS as the power P_1 is raised

beyond the force-balance condition. It may be seen that the zero crossings of ΔF occur at certain positions on the negative and positive z halves of the taper. On the $z < 0$ side, these zero crossings have an antitrapping character, where movement away from the zero-force position leads to a growing force in the direction of movement. On the $z > 0$ side of the taper, the zero crossings have a trapping character, where movement away from the zero position results in a restoring force that pushes the particle back toward the zero position.

C. Calculation of the trapping potential

By numerically performing the integral

$$U(z) = \int_{-\infty}^{z} \Delta F(z')dz', \qquad (3)$$

where $U(z)$ is the potential energy of the particle along the z axis, we can estimate the potential near the zero points for each power in Fig. 2(c). Figure 2(d) shows the results of these calculations. For the case of force balance, $P_1 = 1.7$ mW (solid line), an inflection point rather than a potential minimum occurs. For $P = 2.0$ mW and 2.25 mW, a potential minimum is found at the zero-force position and is seen to move in the positive z direction as the power is increased. The inset of Fig. 2(d) shows ΔF with F^{640} and F^{785} calculated using the approximate theoretical expression of Eq. (1) for a power of $P_1 = 2.5$ mW. Although it shows similar qualitative behavior to the numerically calculated curves, including similar trap depths, it does not agree quantitatively with the numerical calculations. Given that the particle sizes lie outside the Rayleigh regime, this is not surprising. Nonetheless, the theoretical calculation does provide an order-of-magnitude check on the numerical simulations.

As described in the previous section, the trap position is determined by the point where the radiation-pressure forces of the counterpropagating modes balance which, for fixed power P_2, is a monotonic increasing function of P_1. Heuristically, as P_1 increases, the force from the 640-nm mode is able to push the nanoparticle further up the taper before its intensity decays enough that the counterpropagating 785-nm mode force equals it. (Due to its longer wavelength, and thus larger evanescent penetration depth, the 780 nm mode eventually "wins out.") However, the potential depth also becomes smaller as the trapping point moves up the taper, for the simple reason that the evanescent field of *both* modes becomes weaker as the fiber becomes thicker.

IV. EXPERIMENT

We now move on to the experiment. In order to experimentally demonstrate size-selective trapping, we choose particles with a size difference of 50 nm—specifically, 100-

and 150-nm-diameter GNSs. This relatively large size difference means that, assuming constant P_2, trapping occurs for very different P_1 for 100-nm- as opposed to 150-nm-diameter GNSs. This large power difference allows us to unambiguously identify trapping of the two different particle species, despite the fact that they are below the diffraction limit of our microscope. For smaller particle-size differences, it would be necessary to use fluorescently tagged particles with different fluorescence wavelengths in order to confirm size selection, leading to a more complicated experimental setup, along with ambiguities due to absorption and scattering of the fluorescent dye.

The experimental setup is as shown in Fig. 3(a). An optical nanofiber, with a waist diameter of approximately 500 nm and a waist length of 200 μm, is immersed in a droplet of ultrapure water. Colloidal gold nanoparticles (150-nm diameter, Nanopartz A11-150-CIT-DIH; 100-nm diameter, Nanopartz A11-100-CIT-DIH) are then added to this droplet as necessary. Counterpropagating 640- and 785-nm-wavelength guided modes are introduced into the fiber from free-running diode laser sources, with a short-pass filter (SPF) and long-pass filter (LPF) employed to keep counterpropagating light from entering the laser diodes. We polarize both fields before they enter the fiber by passing them through a half-wave plate and a polarizing beam splitter, after which the fields are x polarized, with an intensity controlled by the half-wave plate angle. Light scattered from particles trapped by the nanofiber guided modes is collected by a 20$\times$ objective lens (Olympus LU Plan Fluor, numerical aperture 0.45), attenuated by a neutral density
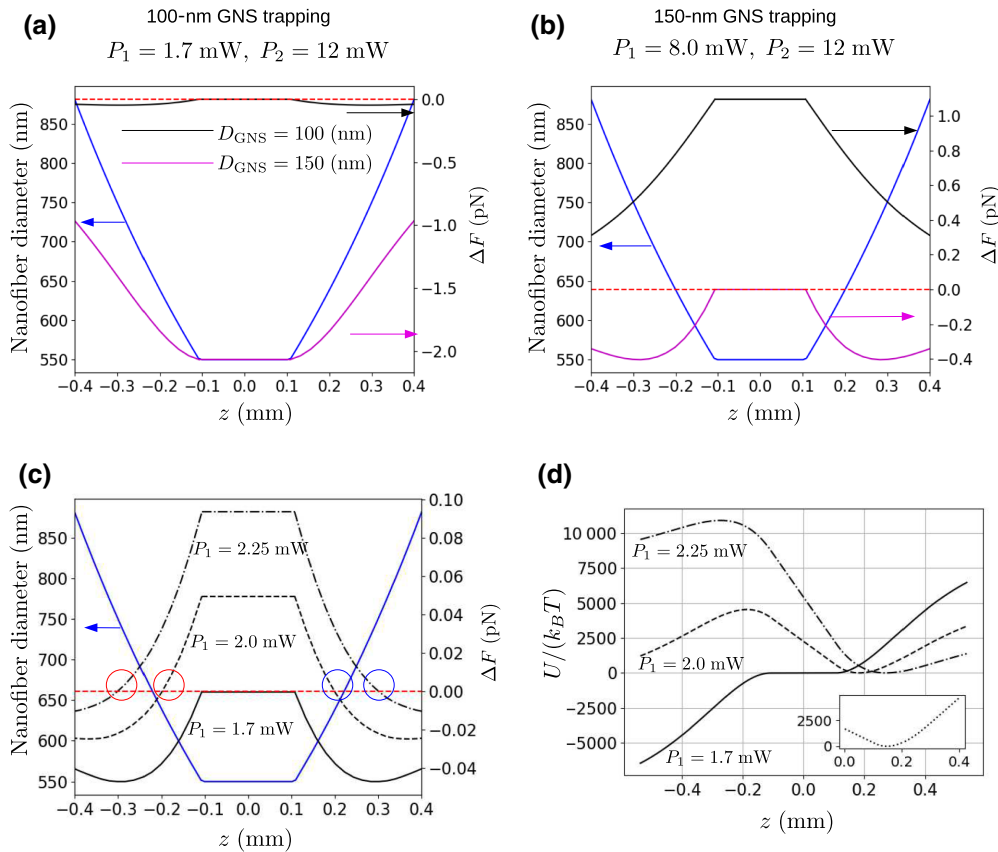

FIG. 2. Numerical predictions. (a),(b) The dependence of the optical forces along the nanofiber axis with $P_2 = 12$ mW (as in the experiments) and given force-balance conditions for a 100-nm-diameter GNS and a 150-nm-diameter GNS, respectively. In all cases, the blue curve shows the nanofiber taper diameter profile (left-hand vertical axis) and the black and magenta curves show the optical forces on 100- and 150-nm-diameter GNSs, respectively (right-hand vertical axis). (c) Variation of the force difference (i.e., total force) on a 100-nm GNS for $P_1 = 1.7$ mW (force-balance condition, solid line), $P_1 = 2.0$ mW (dashed line), and $P_1 = 2.25$ mW (dash-dotted line). As before, the blue curve shows the nanofiber taper diameter profile (left-hand vertical axis). The blue circles show points where stable trapping is possible, whereas red circles show points where antitrapping (i.e., a local potential maximum) exists. (d) The calculated potential energy of a 100-nm GNS as a function of z associated with $P_1 = 1.7$ mW (no trap, solid line), $P_1 = 2.0$ mW (dashed line), and $P_1 = 2.25$ mW (dash-dotted line). For $z > 0$, we see that trapping potential minima occur, whereas for $z < 0$, antitrapping potential maxima occur. Note that the potential minimum has been assigned to zero energy in each case to allow simple comparison of the trap depths. The inset shows a calculation using the approximate theoretical expressions Eq. (1) for a power of $P_1 = 2.5$ mW.
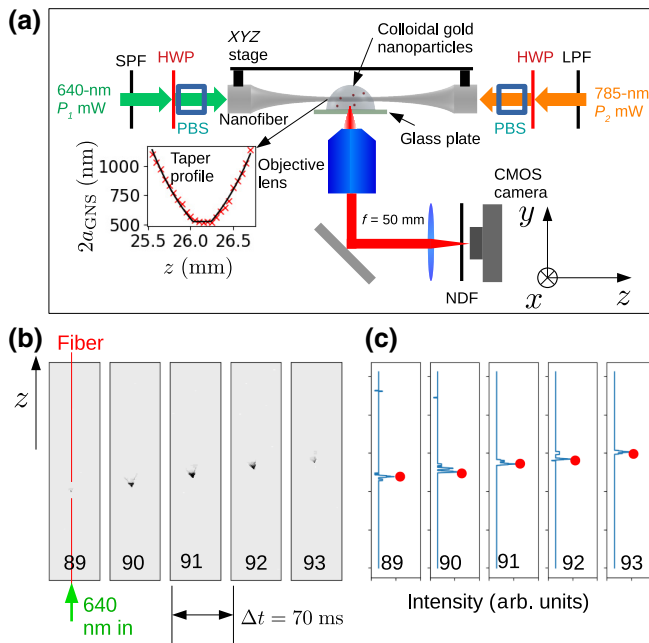
FIG. 3. The experiment. (a) The experimental setup. An optical nanofiber is immersed in a droplet containing colloidal gold nanoparticles. Counterpropagating 640- and 785-nm-wavelength guided modes are introduced into the fiber from diode laser sources, with a short-pass filter (SPF) and long-pass filter (LPF) employed to keep counterpropagating light from entering the laser diodes. Each field passes through a half-wave plate (HWP) and a polarizing beam splitter (PBS) before entering the fiber. Light scattered from particles trapped by the nanofiber guided modes is collected by an objective lens, attenuated by a neutral density filter (NDF) and detected by a CMOS camera. The inset shows the scanning-electron-microscope-measured nanofiber diameter. (b) Example frames from a particle transported along the nanofiber. The frame number is indicated at the bottom of each frame. (c) The 1D data extracted from the frames in (b) by taking only the pictures that lie along the fiber line. The red dots indicate peaks, which are detected and used to create a reduced data set (see text for details).

filter (NDF), focused and then detected by a CMOS camera (Thorlabs DCC1545M). The CMOS-camera-measured intensities I at each pixel constitute our raw data. Note that due to complex scattering of the guided mode light from the nanoparticles and the fiber itself, transported nanoparticles do not have a perfectly circular shape when imaged, even for optimal alignment of the objective lens. Nonetheless, particles can be clearly identified in the data. Example frames are shown in Fig. 3(b), for the situation where $P_1 = 12$ mW and $P_2 = 0$ (i.e., no 785-nm mode). A trapped transported particle is seen as a scattering point that moves along the fiber in the same direction as the 640-nm mode. Because the motion is effectively one dimensional (1D), we can simplify our data considerably by only considering pixels along the line corresponding to the fiber position. Figure 3(c) shows such 1D data for each frame of Fig. 3(b).

Our experimental strategy to observe size-selective trapping using the apparatus described above is to first observe the onset of trapping for a solution containing *only* 150-nm-diameter GNSs. Once the power dependence of transport behavior for 150-nm-diameter GNSs has been characterized, we add 100-nm-diameter colloidal GNSs to the solution and repeat the experiment.

We now move on to our experimental results. First, we consider the case of purely transporting motion for a solution of 150-nm GNSs in the presence of 12 mW of the 785-nm HE_{11} mode alone. After introducing the fiber to a pure water droplet, we add 150-nm GNSs, producing a concentration of 2.6×10^5 particles/μL. We then take 400 frames of data as an avi file using the CMOS camera. The frames are extracted to individual image files and a 1D cross section of each frame is taken along the line corresponding to the fiber position. The combination of this 1D data into a single intensity matrix $I(f, p)$ (where f is an integer specifying the frame and p is an integer specifying the pixel) gives Fig. 4(a), where the horizontal axis is the time in frames and the vertical axis is the distance along the fiber axis in pixels.

We then use a peak-extraction algorithm (PYTHON SciPy module *find_peaks*) to find the estimated position of the particle in each frame, resulting in a reduced data set (l, m) of frame l and pixel position m for each detected peak. These positions are shown by red dots in Fig. 4(b). From the peak data, we use two methods to analyze the particle trajectories along the fiber. The first is the Hough-transform method [36]. Using a polar parametrization of a straight line (ρ, θ), as shown in the inset of Fig. 4(b), the Hough transform creates a spectrum of the peak data in $\rho - \theta$ space. The peaks of the spectrum correspond to lines connecting points in the data, with the largest peak corresponding to the line containing the most points. In this sense, the Hough transform objectively identifies the dominant trajectory in the data. Sample lines found by the Hough transform are shown as dashed black lines in Fig. 4(b) and their θ values are indicated beside each line.

The second method we use is a simple correlation method to find the nearest peaks in consecutive frames, giving the trajectories shown in Fig. 4(c), where the axes are converted to time in s and distance in μm by application of the relevant calibration factors. The calculated mean velocity is shown beside each trajectory. We use this method to find the mean and standard deviation of trajectories in each data set.

The use of the above data-analysis methods allows us to perform an objective analysis of our data rather than focusing on individual trajectories that are subjectively judged to be of interest.

We first perform measurements in the presence of 150-nm-diameter GNSs only, with the same concentration as given above. The power in the 785-nm mode is kept constant at $P_2 = 12$ mW, while the power of the 640-nm mode
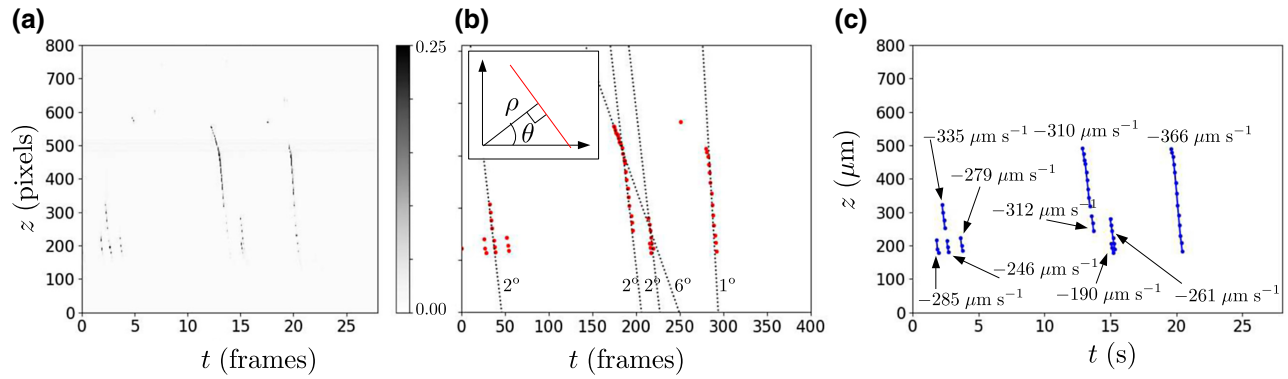
FIG. 4. Experimental data: the transport of 150-nm-diameter GNSs. (a) Combined 1D cross sections for each captured frame in the data set for parameters $P_1 = 0$ mW, $P_2 = 12$ mW, and 150-nm GNSs only. (b) Detected peaks (red points) in the 1D cross-section data along with five lines detected by a Hough analysis of the data (dashed black lines). The inset depicts the polar representation of a line (shown in red) used by the Hough analysis and the detected angle θ is shown beside each detected line. (c) GNS trajectories detected in the data using the correlation technique explained in the text. The associated mean velocity is shown beside each trajectory.

is varied from 0 to 8 mW in 1-mW increments. Immediately after setting the power, 400 frames of data are taken. The results are shown in the upper row of Fig. 5(a) at selected powers. Only transporting trajectories in the direction of the 785-nm-mode propagation are seen until P_1 reaches 8 mW. At this point, trapped particles are observed, as can be clearly seen by the near-horizontal lines in the combined data $I(f, p)$.

After taking the data shown in the upper row of Fig. 5(a), we add a solution of 100-nm-diameter GNSs to the droplet, giving a concentration of 2.2×10^5 particles/μL for the already present 150-nm GNSs and 6.3×10^5 particles/μL for the 100-nm GNSs. No change in the transmitted power of either wavelength mode is observed due to the addition of the solution. We then perform the experiment again at each value of P_1. This time, the onset of particle trapping occurs at approximately 3 mW, as judged by the appearance of multiple near-horizontal particle trajectories [lower row, Fig. 5(a)]. Inspection of the data in the lower row of Fig. 5(a) shows interesting behavior beginning at $P_1 = 4$ mW, where particle trajectories traveling in both directions along the fiber can be seen. For $P_1 = 8$ mW, the data suggest that many particles travel through the region where other particles are trapped. This is due to 100-nm-diameter GNSs being transported along the fiber due to the stronger force they experience from the 640-nm mode. At the same value of P_1, 150-nm GNSs are trapped, and thus the behavior constitutes a type of optical sieve effect but one where either smaller or larger particles can be retained depending on the adjustable optical parameters (for movie data in which this behavior is easier to perceive, see the Supplemental Material [37]).

We note that in the lower row of the 8-mW data, a particle adhering to the fiber is observed. Irreversible particle sticking happens at a rate of approximately once in 2 h and

is distinguishable from particle trapping due to the constant position and constant intensity of the scattering observed. We find that powers in either mode above approximately 12 mW lead to a greater chance of particle sticking, presumably due to the increased radial gradient force pushing particles onto the nanofiber surface.

Figure 5(b) shows the results of a trajectory analysis of the 150-nm-only data, which reveals how the mean trajectory velocity reduces to near zero as P_1 is increased. The error bars show plus and minus one standard deviation of the velocity over the observed trajectories. The standard deviation may be seen to be rather large. The variation in the observed velocities is at least partly attributed to the variation in the particle size, which is specified to be ± 10 nm. Another source of the velocity spread is the azimuthal variation of the intensity of the fundamental mode.

Figure 5(c) shows the angle Θ at the peak of the Hough spectrum for each data set shown in Fig. 5(a). Note that the dominant line in the Hough spectrum for each data set is shown by a black dotted line in Fig. 5(a). The tendency of this value to 90° with the onset of trapping is a quantitative measure of the fact that in the trapping regime, particle trajectories are dominated by long-lifetime trajectories with near-zero velocity. The behavior of Θ is clearly different for the case with only 150-nm-diameter GNSs and the case where both 150- and 100-nm-diameter GNSs are present. We also made similar measurements for a different fiber without polarization control. The Hough angles for these results, shown in Fig. 5(d), show very similar qualitative behavior, suggesting the repeatability of the size-selective trapping behavior. The results also show that polarization control is not necessary to achieve the size-selective trapping effect, which is convenient for practical applications.
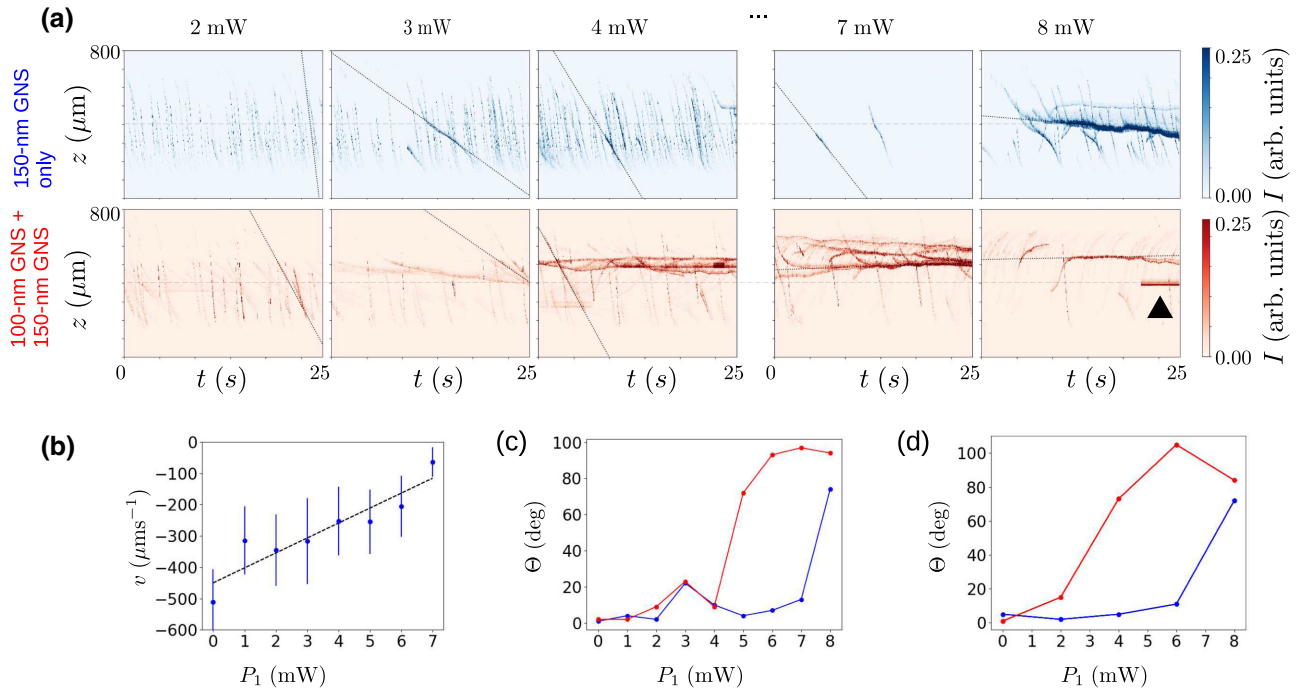
FIG. 5. Experimental data: size-selective trapping. (a) The upper row shows the power dependence of transport in the case where *only* 150-nm-diameter GNSs are present in solution, with P_1 as indicated and P_2 fixed at 12 mW. The onset of trapping is observed at $P_1 = 8$ mW. The lower row shows the power dependence of transport for a mixture of 100-nm-diameter and 150-nm-diameter GNSs. The onset of trapping is now observed at $P_1 = 3$ mW, corresponding to trapping conditions for the 100-nm-diameter GNSs. In each case, a black dotted line shows the dominant line of the Hough spectrum, while dashed horizontal lines indicate the nominal position of the nanofiber center. The black arrow in the lower row of the 8-mW data indicates a particle stuck to the fiber surface. This is ignored for the purposes of the Hough analysis. For movie file data for similar parameters, see the Supplemental Material [37]. (b) The power dependence of the mean velocity for trajectories detected in each data set shown in the upper row of (a). The error bars show plus or minus one standard deviation. (c) The angle Θ of the top-ranked line detected by Hough analysis for each data set shown in the upper row of (a) (blue points) and the bottom row of (a) (red points). (d) The same as (c), but for a data set where there is no control over the polarization of the fields entering the nanofiber.

V. DISCUSSION

Let us compare our experimental results with the numerical predictions. First, we consider the qualitative predictions. According to the principle of the two-color technique, the onset of trapping will occur near to the nanofiber center [i.e., ± 100 μm about the dashed line shown in Fig. 5(a), where the nanofiber diameter is constant], as seen in the case of 150-nm-diameter GNSs only when $P_1 = 8$ mW and also for $P_1 = 3$ mW when 100-nm-diameter GNSs are present. As P_1 is increased, the position of trapping should move in the positive z direction and no trapping should be observed below the nanofiber center. Our experimental results are completely in line with this theoretical prediction. Most importantly, the onset of trapping for 100-nm GNSs should occur at a much lower power for 100-nm GNSs than for 150-nm GNSs. Again, our data are consistent with this prediction.

In terms of quantitative predictions, the onset of trapping is seen to occur at $P_1 = 8$ mW for 150-nm-diameter GNSs only, in agreement with the numerical prediction of

8.0 mW. When 100-nm GNSs are present, the numerics predict an onset of trapping at 1.7 mW, i.e., 2.0 mW at the 1 mW resolution of the experiment. The onset of trapping is seen at 3 mW in experiments. The discrepancy between the numerical predictions and the experimental result may be due to a number of effects, including the difference in plasmon-resonance line shape for the experimentally used 100-nm GNSs relative to the ideal simulated versions, along with nonoptical effects such as heating (not included in our simulations). The numerics also predict that the taper-trapping region should be between 100 and 300 μm from the nanofiber center, in line with what is observed experimentally in the case where 100-nm GNSs are present.

Although the evidence for size-dependent trapping and the optical sieve effect accumulated here is necessarily indirect, due to the subwavelength size of the nanoparticles, the above agreement between multiple aspects of theory, numerics, and experiment provides strong support for our interpretation. We also note that using an objective measure of the dominant trajectory in each data

set (i.e., the Hough analysis), rather than relying on our visual impression of the data, clearly shows the expected difference between the onset of trapping in the case where only 150-nm GNSs are present, compared to the case where both 100- and 150-nm-diameter GNSs are in the solution.

In future experiments, we anticipate that similar size-selective effects could be achieved for nonmetallic particles, using, for example, whispering-gallery resonances or other size-dependent resonance effects. Furthermore, our current demonstration is for a 50 nm difference in particle diameters but simple calculations suggest that selective trapping for diameter differences down to at least 20 nm is possible for the current experimental configuration. To give a concrete example, let us require $P_1 < P_2 = 12$ mW and at least 1 mW difference between trapping conditions for different species as used in the current experiment. Now, the ratio R shown in the inset of Fig. 1(a) tells us the ratio of the forces for 640- and 785-nm-wavelength modes, respectively, at constant power. Therefore, a 100-nm-diameter nanoparticle and a 120-nm-diameter nanoparticle have trapping powers of $P_1 = P_2/R = 12/8.4 = 1.4$ mW and $P_1 = P_2/R = 12/4.5 = 2.7$, respectively, and thus can in principle be selectively trapped or transported using the technique presented here. A similar argument shows that if we allow the power difference for trapping of different species to be 0.5 mW, then a diameter difference of approximately 10 nm can be resolved.

VI. CONCLUSION

In conclusion, we demonstrate the size-dependent trapping and transport of 100- and 150-nm-diameter gold nanospheres radially trapped near a submicron-diameter optical-fiber taper. In particular, it is possible to trap one species of particle at a certain point on the fiber taper while the other species is transported through the trapping region—an effect that may be termed an optical sieve. The simplicity and robustness of the experimental setup used here makes it an excellent candidate for practical nanoparticle sorting applications and we anticipate uses for this technique in size-selective manipulation of various types of particles, including bionanoparticles.

ACKNOWLEDGMENT

[1] X. Wang, J. Zhuang, Q. Peng, and Y. Li, A general strategy for nanocrystal synthesis, Nature **437**, 121 (2005).

[2] S. Ryu, K. Lee, S. H. Hong, and H. Lee, Facile method to sort graphene quantum dots by size through ammonium sulfate addition, RSC Adv. **4**, 56848 (2014).

[3] J. Wei, J. Qiu, L. Ren, K. Zhang, S. Wang, and B. Weeks, Size sorted multicolor fluorescence graphene oxide quantum dots obtained by differential velocity centrifugation, Sci. Adv. Mater. **6**, 1052 (2014).

[4] Y. Morita, T. Takimoto, H. Yamanaka, K. Kumekawa, S. Morino, S. Aonuma, T. Kimura, and N. Komatsu, A facile and scalable process for size-controllable separation of nanodiamond particles as small as 4 nm, Small **4**, 2154 (2008).

[5] P. Van Hee, M. Hoeben, R. Van der Lans, and L. Van der Wielen, Strategy for selection of methods for separation of bioparticles from particle mixtures, Biotechnol. Bioeng. **94**, 689 (2006).

[6] J. C. Yeo, Z. Wang, and C. T. Lim, Microfluidic size separation of cells and particles using a swinging bucket centrifuge, Biomicrofluidics **9**, 054114 (2015).

[7] Q.-Y. Lin, E. Palacios, W. Zhou, Z. Li, J. A. Mason, Z. Liu, H. Lin, P.-C. Chen, V. P. Dravid, K. Aydin, *et al.*, DNA-mediated size-selective nanoparticle assembly for multiplexed surface encoding, Nano Lett. **18**, 2645 (2018).

[8] J. Xuan, *Size-Based Separation of Bioparticles Using Planar Nanofluidic Devices* (Brigham Young University, Provo, 2013).

[9] K. Svoboda and S. M. Block, Biological applications of optical forces, Annu. Rev. Biophys. Biomol. Struct. **23**, 247 (1994).

[10] M. Carta, R. Malpass-Evans, M. Croad, Y. Rogan, J. C. Jansen, P. Bernardo, F. Bazzarelli, and N. B. McKeown, An efficient polymer molecular sieve for membrane gas separations, Science **339**, 303 (2013).

[11] B. B. Stogin, L. Gockowski, H. Feldstein, H. Claure, J. Wang, and T.-S. Wong, Free-standing liquid membranes as unusual particle separators, Sci. Adv. **4**, eaat3276 (2018).

[12] F. Nan and Z. Yan, Sorting metal nanoparticles with dynamic and tunable optical driven forces, Nano Lett. **18**, 4500 (2018).

[13] M. Righini, A. S. Zelenina, C. Girard, and R. Quidant, Parallel and selective trapping in a patterned plasmonic landscape, Nat. Phys. **3**, 477 (2007).

[14] M. Ploschner, T. ČiŽmár, M. Mazilu, A. Di Falco, and K. Dholakia, Bidirectional optical sorting of gold nanoparticles, Nano Lett. **12**, 1923 (2012).

[15] T. Kudo and H. Ishihara, Proposed Nonlinear Resonance Laser Technique for Manipulating Nanoparticles, Phys. Rev. Lett. **109**, 087402 (2012).

[16] T. Wada, H. Fujiwara, K. Sasaki, and H. Ishihara, Proposed method for highly selective resonant optical manipulation using counter-propagating light waves, Nanophotonics **9**, 3335 (2020).

[17] S. Kawata and T. Tani, Optically driven Mie particles in an evanescent field along a channeled waveguide, Opt. Lett. **21**, 1768 (1996).

[18] L. Ng, B. Luff, M. Zervas, and J. Wilkinson, Propulsion of gold nanoparticles on optical waveguides, Opt. Commun. **208**, 117 (2002).

[19] S. Skelton, M. Sergides, R. Patel, E. Karczewska, O. Marago, and P. Jones, Evanescent wave optical trapping

and transport of micro-and nanoparticles on tapered optical fibers, J. Quant. Spectrosc. Radiat. Transfer **113**, 2512 (2012).

[20] A. Maimaiti, V. G. Truong, M. Sergides, I. Gusachenko, and S. N. Chormaic, Higher order microfibre modes for dielectric particle trapping and propulsion, Sci. Rep. **5**, 9077 (2015).

[21] T. Yoshino, D. Yamaura, M. Komiya, M. Sugawara, Y. Mitsumori, M. Niwano, A. Hirano-Iwata, K. Edamatsu, and M. Sadgrove, Optical transport of sub-micron lipid vesicles along a nanofiber, Opt. Express **28**, 38527 (2020).

[22] Y. Tanaka and K. Sasaki, Optical trapping through the localized surface-plasmon resonance of engineered gold nanoblock pairs, Opt. Express **19**, 17462 (2011).

[23] C. Min, Z. Shen, J. Shen, Y. Zhang, H. Fang, G. Yuan, L. Du, S. Zhu, T. Lei, and X. Yuan, Focused plasmonic trapping of metallic particles, Nat. Commun. **4**, 2891 (2013).

[24] H. Fujiwara, K. Yamauchi, T. Wada, H. Ishihara, and K. Sasaki, Optical selection and sorting of nanoparticles according to quantum mechanical properties, Sci. Adv. **7**, eabd9551 (2021).

[25] Y. Shi, S. Xiong, L. K. Chin, J. Zhang, W. Ser, J. Wu, T. Chen, Z. Yang, Y. Hao, B. Liedberg, P. H. Yap, D. P. Tsai, C.-W. Qiu, and A. Q. Liu, Nanometer-precision linear sorting with synchronized optofluidic dual barriers, Sci. Adv. **4**, eaao0773 (2018).

[26] F. Le Kien, V. I. Balykin, and K. Hakuta, Atom trap and waveguide using a two-color evanescent light field around a subwavelength-diameter optical fiber, Phys. Rev. A **70**, 063403 (2004).

[27] J. J. Xiao, H. H. Zheng, Y. X. Sun, and Y. Yao, Bipolar optical forces on dielectric and metallic nanoparticles by evanescent wave, Opt. Lett. **35**, 962 (2010).

[28] T. Čižmár, V. Garcés-Chávez, K. Dholakia, and P. Zemánek, Optical conveyor belt for delivery of submicron objects, Appl. Phys. Lett. **86**, 174101 (2005).

[29] T. Čižmár, V. Kollárová, Z. Bouchal, and P. Zemánek, Sub-micron particle organization by self-imaging of non-diffracting beams, New J. Phys. **8**, 43 (2006).

[30] D. B. Ruffner and D. G. Grier, Optical Conveyors: A Class of Active Tractor Beams, Phys. Rev. Lett. **109**, 163903 (2012).

[31] O. Brzobohatỳ, V. Karásek, M. Šiler, L. Chvátal, T. Čižmár, and P. Zemánek, Experimental demonstration of optical transport, sorting and self-arrangement using a 'tractor beam', Nat. Photonics **7**, 123 (2013).

[32] D. E. Fernandes and M. G. Silveirinha, Single-Beam Optical Conveyor Belt for Chiral Particles, Phys. Rev. Appl. **6**, 014016 (2016).

[33] M. Sadgrove, S. Wimberger, and S. N. Chormaic, Quantum coherent tractor beam effect for atoms trapped near a nanowaveguide, Sci. Rep. **6**, 28905 (2016).

[34] K. Svoboda and S. M. Block, Optical trapping of metallic Rayleigh particles, Opt. Lett. **19**, 930 (1994).

[35] K. Okamoto, *Fundamentals of Optical Waveguides* (Academic Press, San Diego, 2006).

[36] P. V. Hough, Method and means for recognizing complex patterns, U.S. Patent 3,069,654 (1962).

[37] See the Supplemental Material at http://link.aps.org/supple mental/10.1103/PhysRevApplied.16.044034 for an annotated example of the raw movie data.